Investigation of deep levels in CdZnTeSe crystal and their effect on the internal electric field of CdZnTeSe gamma-ray detector

M Rejhon, V Dědič, L Beran, U N Roy, J Franc and R B James

***Abstract*—A study of deep levels in CdZnTeSe radiation-detection materials is presented. The approach relies on electrical methods that combine time and temperature evolution of the electric field and electric current after switching on the bias voltage. Two optical methods were also applied to study the deep levels. The first method utilizes the temperature and temporal analysis of the electric-field evolution after switching off an additional light illuminating the sample at a wavelength of 940 nm. The second method involved measuring of the electric-field spectral dependence during near infrared illumination. The results are compared with those obtained with high-quality CdZnTe detector-grade material. We conclude that the introduction of Se into the lattice leads to a shift of the second ionization level of the Cd vacancy towards the conduction band, as predicted recently by first-principles calculations based on screened hybrid functionals.**

***Index Terms*—CdZnTeSe, deep levels, energy bandgap, electric field dynamics, Pockels effect**

I. INTRODUCTION

THE CdTe and CdZnTe materials have been effectively used for the production of X-ray and gamma-ray detectors operating at room temperature for applications in medical imaging, security and astrophysics [1], [2], [3], [4]. However, there are still several drawbacks that limit the yield of detector-grade material in the crystals. These include mainly the presence of sub-grain boundaries, Te inclusions/precipitates and compositional inhomogeneity arising from the non-unity segregation coefficient of Zn in the CdTe matrix [1], [5], [6], [7], [8].

The sub-grain boundaries are formed during the post-growth ingot cooling process due to the poor thermo-physical properties of the melt and the solidified material. These boundaries act as trapping centres and affect the electrical and transport properties of the material [9], [10].

The Te inclusions/precipitates originate from the growth process under a Te-rich atmosphere. These secondary phases affect the quality and performance of the CdTe and CdZnTe (CZT) depending on their concentration and size [6]. Also, Te secondary phases act as trapping and recombination centres and are responsible for a degradation of the material's detection parameters [11], [12].

Recently it has been shown that the addition of Se in the matrix results in an effective lattice hardening and a decreased Te inclusion/precipitate concentration with increased Se content. It was observed that CdZnTeSe (CZTS) crystals exhibit better crystallinity than CZT, which can lead to a larger yield of high-quality material with comparable electrical and spectroscopic properties as for CdTe and CZT materials [13].

In the current study, we seek to determine the deep levels that participate in space-charge formation and determine the internal electric-field profile and its dynamics after application of a bias and incident radiation flux. The results are compared with our previous study of high-quality CdZnTe detector material to access the impact of Se on the defect structure. Two optical methods were applied to study the deep levels. The first method was the temperature and temporal analysis of the electric-field evolution after bias application and after switching off an additional light illuminating the sample at a wavelength at 940 nm. The light source with this photon energy forms a positive space charge in the sample, which causes the optically induced polarization. The second method was the scanning of the electric-field response to incident infrared (NIR) illumination in the range of $900 - 1800$ nm.

II. EXPERIMENTAL

For this study a CZTS sample with 10% Zn and 4% Se content has been chosen. The material was doped with In in the ppm range and grown by the travelling heater method. The sample dimensions are $6.50 \times 5.30 \times 2.68$ mm^3. The sample surfaces were mechanically polished with Al_2O_3 abrasive (surface RMS 2 nm) without any further chemical treatment. Gold and indium contacts were deposited on the large opposite sides by evaporation. The gold contact was equipped with a guard ring to separate the effects of the bulk and surface leakage currents during electrical measurements.

The sample's energy band-gap was evaluated by a spectroscopic ellipsometry measurement using a commercial JA Woollam Co. RC2 ellipsometer. The ellipsometry was measured in reflection mode with three incident angles of 55° , 60° and 65°, respectively. The range of spectral photon energies was between 0.80 and 6.42 eV.

The dependence of a steady-state electric field on the photon energy for NIR illumination was measured using the Pockels effect. A standard setup consisted of a test light, two polarizers

M Rejhon,V Dědič, L Beran and J Franc are with Charles University, Faculty of Mathematics and Physics, Institute of Physics, Ke Karlovu 5, CZ-121 16 Prague 2, Czech Republic, e-mail: rejhonm@karlov.mff.cuni.cz

U N Roy is with Nonproliferation and National Security Department, Brookhaven National Laboratory, Upton, New York, USA.

R B James is with Savannah River National Laboratory, Aiken, South Carolina 29808, USA.

Manuscript received August, 2018.

and an InGaAs camera. The sample was placed between two crossed polarizers, and the test light operating at a wavelength of 1550 nm was passed through the sample. The transmitted light $I(x, y)$ was detected by an InGaAs camera. The distribution of the internal electric field is $E(x, y) \approx \sqrt{I(x, y)}$. More details about the measurement setup are provided in our previous articles [14], [15].

The light from the monochromator in the range $900 - 1800$ nm was used to scan the spectral dependence of the internal electric field in the sample with a step size of 25 nm. The monochromatic incident light had a constant photon flux of 1.0×10^{15} photons $\mathrm{cm}^{-2}\mathrm{s}^{-1}$, and the measurements were carried out at room temperature (300 K). This technique allows one to determine the deep levels in the detector due to the measurement of the change of the internal space charge [15], [16].

The temporal and temperature evolutions of the electric field after application of the bias and switching off the LED at 940 nm with a photon flux of 5.5×10^{15} photons $\mathrm{cm}^{-2}\mathrm{s}^{-1}$ were measured. The electric field was measured using the same standard setup as for the previous experiment. The incident light at the wavelength of 940 nm forms a positive space charge in the CdTe and CZT detectors, which induced polarization of the detectors [15], [17], [18]. The return of the electric field to the original state (i.e., without illumination) based on the thermal emission of charge carriers from the traps allows determination of the deep levels responsible for the polarization [14], [19]. An analysis of the time and temperature evolution of the electric current after switching on the bias was also employed.

The sample was mounted in a cryostat, and the temperature was varied between $280 - 330$ K using a thermoelectric cooler with a temperature step of 5 K. The measurements were made in an argon atmosphere (1000 mbar).

III. RESULTS AND DISCUSSION

A. *Ellipsometry*

The spectroscopic ellipsometry measurements performed on the CZTS sample allows determination of the energy band-gap. We also measured the energy band-gap of the CZT material to determine the energy shift of the band-gap caused by the addition of Se. The experimental ellipsometry data were fitted by a theoretical model describing the CZTS/CZT materials. The CZTS/CZT materials were parametrized by a sum of Lorentz oscillators [20], [21]. The determined optical refractive index of CZTS bulk and CZT bulk is shown in figure 1. The evaluated energy band-gap of CZTS is $E_G^{CZTS} = 1.52$ eV, and for CZT it is $E_G^{CZT} = 1.59$ eV.

B. *Bias application*

The time evolution of the electric field in the sample after bias application was measured in the temperature range between $280 - 330$ K. The selected profiles of the electric field are shown in figure 2(a). The electric field in the steady state indicates the formation of a positive space charge in the sample.

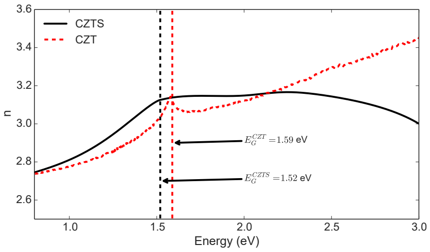

Fig. 1. The optical refractive index of CZTS material (black solid line) and CZT material (red dashed line). The determine energy bandgaps are marked by dashed lines.

The time evolution of the electric field under the cathode at 300 K is plotted in figure 2(b). The time evolution of the space charge Q was computed for a better understanding of the electric field development by the formula [19]

$$Q = \varepsilon S(\mathcal{E}_{cathode} - \mathcal{E}_{anode}). \tag{1}$$

Here, ε is the absolute permittivity, S is the sample area, and $\mathcal{E}_{cathode,anode}$ is the electric field at the cathode and the anode, respectively.

In our previous study of CZT [19], we observed the undershoot in the evolution of the electric field under the cathode, but the space charge was described by a single-exponential function. It indicates a critically damped oscillation of the electric field caused by local space-charge fluctuations by one principal deep level. However, in the case of CZTS, the time evolution of the space charge (figure 2(c)) exhibits a similar undershoot as the evolution of the electric field (figure 2(b)). This effect cannot be explained by just one deep level. Therefore, we apply fitting of the experimental curves by a double-exponential function, which describes the influence of two dominant deep levels.

The activation energies of the levels E_i were evaluated from the temperature dependence of the time constants τ_i describing the time evolution of the electric field under the cathode and space charge evolution by an Arrhenius equation

$$\ln(\tau_i T^2) = \frac{E_i}{k_B T} + \ln\left(\frac{C}{\sigma_i}\right); \quad C = \frac{h^3}{16 m^*_{e(h)} \pi k_B^2}, \tag{2}$$

where T is the absolute temperature, k_B is the Boltzmann, h is the Planck constant, $m^*_{e(h)}$ is the effective mass of electrons (holes) and σ_i is the capture cross-section of the level.

An activation energy of 0.82 ± 0.04 eV was determined from the temperature dependence of τ_1 describing the increase of the electric field under the cathode (black squares in figure 2(d)). This process can be described by the thermal transition of electrons from the deep level to the conduction band resulting in the observed increase of the positive space charge. Therefore, the activation energy was assigned to the deep level $E_1 = E_c - 0.82 \pm 0.04$ eV with electron capture cross section $\sigma_n = 1.0 \times 10^{-11}$ cm^2.

The time constant τ_2 describes the decrease of the electric field under the cathode, which correlates with the electron transition from the valence band to the deep level. The data are plotted as black circles in figure 2(d). The determined deep

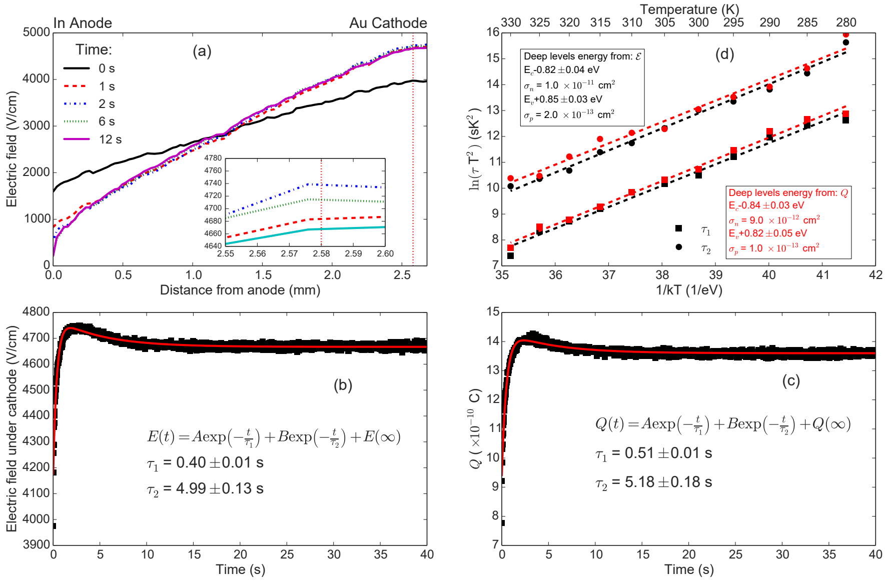

Fig. 2. The graph (a) shows the selected profile of electric field after bias application. The red dotted line shows the distance from the cathode. The time evolution of the electric field is plotted on the graph (b). The experimental data (black square) are fitted by a double-exponential function (red line) with time constants $\tau_1 = 0.40 \pm 0.01$ s and $\tau_2 = 4.99 \pm 0.13$ s. The space charge evolution in time is shown in graph (c). The data are shown as black squares, and the double-exponential fit with time constants is plotted as a red line. The graph (c) includes the determined time constants $\tau_1 = 0.51 \pm 0.01$ s and $\tau_2 = 5.18 \pm 0.18$ s. The Arrhenius diagram is plotted on the graph (d). The observed deep level energies are $E_c - 0.82 \pm 0.04$ eV with electron capture cross-section $\sigma_n = 1.0 \times 10^{-11}$ cm^2 and $E_v + 0.85 \pm 0.03$ eV with hole capture cross-section $\sigma_p = 2.0 \times 10^{-13}$ cm^2 from time constants describing the electric-field evolution. The deep levels determined from space charge evolution are $E_c - 0.84 \pm 0.03$ eV with electron capture cross-section $\sigma_n = 9.0 \times 10^{-12}$ cm^2 and $E_v + 0.82 \pm 0.05$ eV with hole capture cross-section $\sigma_p = 1.0 \times 10^{-13}$ cm^2.

level is $E_2 = E_v + 0.85 \pm 0.03$ eV with hole capture cross section $\sigma_p = 2.0 \times 10^{-13}$ cm^2.

The Arrhenius analysis was performed on time constants describing the space-charge evolution. The time constant τ_1 related to the increase of positive space charge leads to the deep level $E_1 = E_c - 0.84 \pm 0.03$ eV with electron capture cross section $\sigma_n = 9.0 \times 10^{-12}$ cm^2 (red squares in figure 2(d)). The analysis of the time constant τ_2 (red circles in figure 2(d)) provides the deep level $E_2 = E_v + 0.82 \pm 0.05$ eV with hole capture cross section $\sigma_p = 1.0 \times 10^{-13}$ cm^2 due to the decreasing of the positive space charge. We conclude that both methods of evaluation (electric field and total space charge) lead to the same results within the expected experimental error.

Figures 3(a-c) show the time evolutions of the measured electric current after switching on the bias at three different temperatures 290, 300 and 310 K. The current decreases within the first two seconds with time constant $\tau_1 = 0.38$ sec at 300 K. It is the same time constant with which the electric field below the cathode increases (figure 2(b)). The buildup of positive space charge is thus accompanied with a decrease of the electric current. The Arrhenius analysis the time constant τ_1 (figure 3(d)) gives an energy of 0.65 eV and carrier capture cross-section of 1×10^{-15} cm^2. This energy is complementary to the electron trap $E_1 = E_c - 0.83$ eV. The sum $0.83 + 0.65$ eV agrees within the experimental error with the band-gap of the material at 1.52 eV as measured by ellipsometry. This energy is therefore connected with thermally activated emission of holes from the valence band to the level causing that the absolute value of the electric current immediately after switching on the bias increases with temperature (from 7.5 nA at 290 K to 38 nA at 310 K).

In summary, within the first two seconds after application of the bias, the positive space charge is built up by electron transitions from this level to conduction band. At the same time free holes are trapped at the level decreasing the electric current, which therefore seems to be composed mainly from holes. After the initial decrease the electric current starts to increase with time constant $\tau_2 = 3.74$ sec at 300 K. An Arrhenius analysis of this time constant gives an activation energy of 0.92 eV. With a similar time activation energy and time constant, the electric field below the cathode decreases (positive space charge decreases - figure 2(c)). Therefore, we conclude that the observed increase of the electric current is caused by the emission of holes at the level $E_2 = E_v + 0.83$ eV. Corresponding transitions of electrons from the valence band to the level cause the decrease of the positive space charge.

Additional analysis of time and temperature evolution of the electric current fully confirmed the conclusions obtained from evaluation of the electric-field dependences. Furthermore, the capture cross-section for holes at the electron trap $E_1 = E_c - 0.83$ eV could be evaluated from the data.

C. *Infrared spectral scanning*

The dependence of the selected electric-field profiles on the NIR illumination from the monochromator is shown in figure 4(a). The electric-field profile without illumination linearly increases from the anode to the cathode, which indicates a positive space charge in the sample volume. The below band-gap NIR light from the monochromator penetrates through the whole sample volume. The penetrated light can affect the

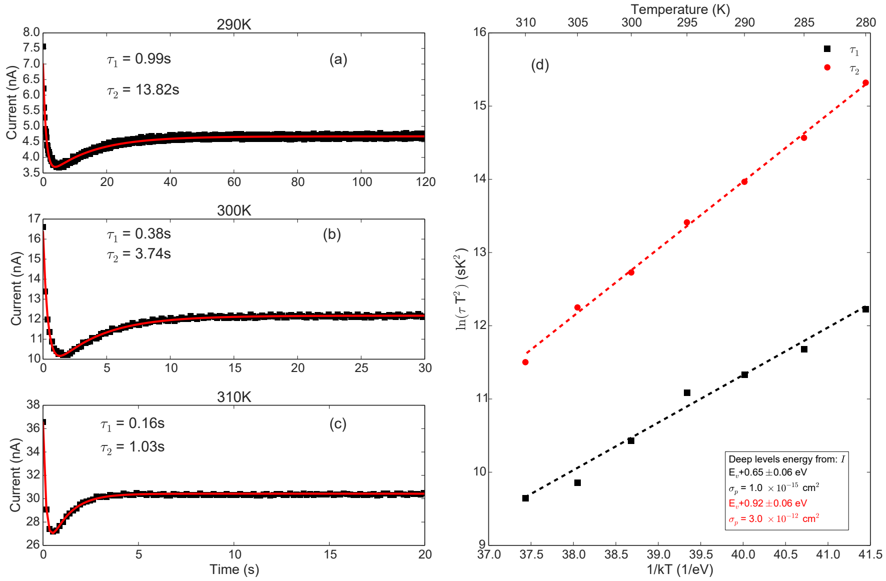

Fig. 3. The graphs (a-c) show the time evolution of the measured electric current after switching on the bias at three different temperatures 290 (a), 300 (b) and 310 K (c). The Arrhenius diagram is plotted on graph 3(d). The observed deep-level energies are $E_v + 0.65 \pm 0.06$ eV with hole capture cross-section $\sigma_p = 1.0 \times 10^{-15}$ cm^2 and $E_v + 0.92 \pm 0.06$ eV with hole capture cross-section $\sigma_p = 3.0 \times 10^{-12}$ cm^2.

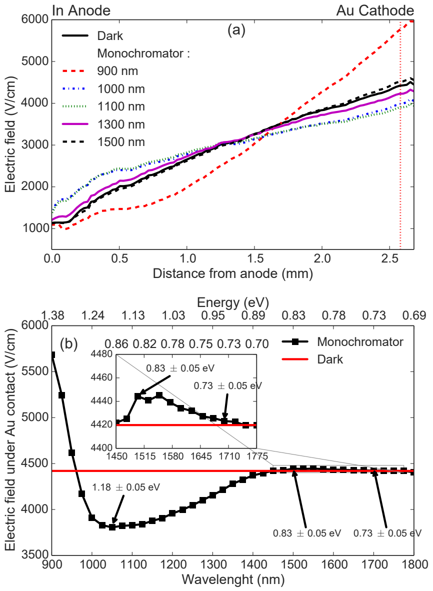

Fig. 4. The profiles of the electric field with and without illumination from the source of the monochromator light (a). The applied voltage was 800 V on the In contact and the temperature was 300 K. The red dotted line demonstrates the distance from the cathode where the electric field was cut and plotted showing the dependence on illumination wavelength on the bottom figure (b). The inset graph shows the area in the range of $1450 - 1775$ nm. The arrows mark the change of the electric field under the cathode induced by the optical transition. The determined deep levels are 0.73, 0.83 and 1.18 eV with a 0.05 eV error.

occupation of deep levels, which leads to a change of the space-charge distribution and modification of the electric-field profile.

The dependence of the electric field under the cathode (0.1 mm from cathode) is shown in figure 4(b) for a step of 25 nm. The illumination at 1725 nm (0.73 eV) causes a slight increase of the electric field under the cathode due to transitions of electrons from the deep level to the conduction band $E_3 = E_c - 0.73$ eV. This transition causes an increase of the positive space charge. It leads to the increase of the electric field under the cathode. Other optically induced electron transitions affecting the electric field start at 1500 nm (0.83 eV). The decrease of the electric field under the cathode indicates a decrease of the positive space charge in the sample. It corresponds to transitions of electrons from the valence band to the deep level $E_2 = E_v + 0.83$ eV. The electric field under the cathode starts to increase at 1050 nm (1.18 eV) due to electron transitions from the deep level at $E_4 = E_c - 1.18$ eV to the conduction band. This transfer forms the positive space charge in the sample.

D. Time and temperature evolution of the electric field after switching off the LED at 940 nm

The time evolution of the electric field after switching off the LED at the wavelength of 940 nm was monitored. The illumination by 940-nm light causes an increase of the positive space charge in the sample. The electric field returns to the dark condition (steady state) after switching off the 940-nm LED. It means that the generated positive space charge is reduced due to the thermally activated electron transitions from the valence band to the deep level or due to the non-thermally activated electron capture from the conduction band to the deep level.

The selected electric-field profiles at 0, 1, 5, 10 and 30 seconds after switching off the LED operating at 940 nm are shown in figure 5(a). The electric-field profile at 0 second indicates a dead layer under the In anode due to the generated positive space charge.

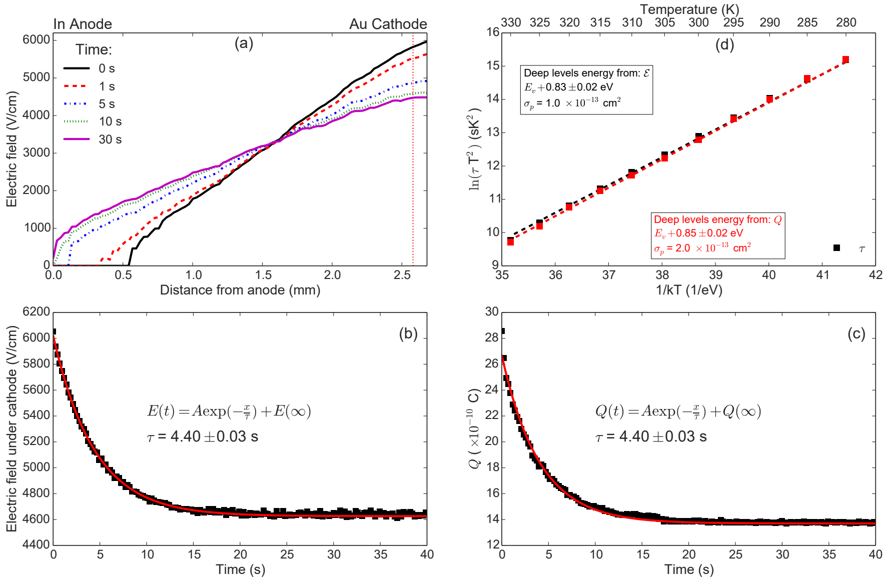

Fig. 5. The graph (a) shows the selected profiles of the electric field after switching off the LED at 940 nm at a temperature of 300 K and bias of 800 V on the In contact. The red dotted line shows the distance from cathode, and the time evolution of the electric field is plotted in graph (b). This graph shows a mono-exponential decay of the electric field under the cathode (black square) with the mono-exponential fit (red line). The graph is supplemented by the determined time constant $\tau = 4.40 \pm 0.03$ s. The computed space charge is plotted on the graph (c) as black squares with the single exponential fit (red line). The Arrhenius diagram is plotted on the graph (d). The observed deep level energy is $E_v + 0.83 \pm 0.02$ eV ($E_v + 0.85 \pm 0.02$ eV) with hole capture cross-section of $\sigma_p = 1.0 \times 10^{-13}$ cm^2 ($\sigma_p = 2.0 \times 10^{-13}$ cm^2) from the evolution of the electric field under the cathode (space charge evolution).

The corresponding time evolution of the electric field under the cathode is depicted in figure 5(b), and the computed space charge according to equation (1) is plotted in figure 5(c). Both time dependences exhibit a single exponential decay.

The activation energy of thermally activated transitions is identified using an Arrhenius plot (figure 5(d)). The transition from the valence band to the deep level $E_2 = E_v + (0.83 \pm 0.02)$ eV with a capture cross-section of $\sigma_p = 1 \times 10^{-13}$ cm^2 is evaluated from the time constant of the corresponding electric-field evolution. The temperature dependence of the time constant describing the space-charge evolution leads to the deep level $E_2 = E_v + (0.85 \pm 0.02)$ eV with a capture cross-section of $\sigma_p = 2 \times 10^{-13}$ cm^2.

The main deep level in the CZTS sample responsible for the optically induced polarization is at $E_2 = E_v + 0.83$ eV. The incident light at 940 nm caused the electron transitions from this level to the conduction band. It increased the positive space charge, which leads to the polarization of the detector. After switching off the illumination at 940 nm, the electron returns to this deep level from the valence band. It causes the decrease of the induced positive space charge. We conclude that both the energy and capture cross-section of this deep level are the same as those evaluated after bias application.

E. Comparison with CdZnTe

The observed deep levels in CZTS material are shown in the energy scheme (figure 6(a)). The CZT deep levels evaluated by the same approach [14], [15], [16] are presented in figure 6(b). The deep level at $E_4 = E_c - 1.18$ eV was evaluated from spectral infrared scanning in the CZTS material. This deep level is responsible for strong optically induced polarization. The CZT material demonstrates the deep level at $E_c - 1.10$ eV determined by the same method [15], [16]. Both start to form positive space charge in the material, so we assume that the levels have the same origin. Kim [22] assigned this deep level to dislocations induced by Te inclusions/precipitates. Castaldini [23] attributed this energy level at 1.1 eV below the conduction level to a positively charged tellurium vacancy. Du et al [24] calculated the energy of a deep donor state of Te antisite corresponding to the $+2/0$ charge state 0.35 eV above the valence band. The calculated levels of the vacancy V_{Te} are approximately 0.9 eV and 1.1 eV. Transitions ascribed to both the Te antisite and Te vacancy are within the experimental error in the range of energies observed in our previous article [15] and in the current paper. Based on the published experimental data and theoretical models it is therefore probable, that the observed energy levels are connected to Te atoms that migrated to Cd position (Te antisite) or to the surface (Te vacancy). It should be noted that transitions in this energy range are in the literature often ascribed also to dislocations [25] and deep impurities. An extended literature overview to this topic can be found in ref [26]. We assume that the observed energy shift is caused by the addition of Se content.

It is apparent that the activation energies of electrons from deep levels E_3 and E_4 to the conduction band are higher in CZTS by $30-80$ meV when compared to CZT. The activation energy of electrons from the valence band to the deep level E_2 is also higher by approximately 50 meV in case of CZTS. At the same time the energy band of CZTS is smaller by 70 meV compared to CZT (figure 1). It means that the observed shifts of energies in CZTS when compared to CZT cannot be simply explained by the change of the band-gap after introduction of

Se in the lattice. While the change of energies of the principal deep levels may seem relatively small, it can significantly influence occupations of these levels if they are close to the Fermi energy, and in this way affect the stability of the Fermi level along the ingot as well as trapping and recombination of free carriers. A detailed study of the impact of these energy-level shifts will be a focus of our future research.

The deep level $E_2 = E_v + 0.83$ eV in CZTS has probably the same origin as the level $E_v + 0.77$ eV in CZT [14]. This level was assigned to the second ionized state of cadmium vacancy by Castaldini [23]. It is responsible for both a thermally and an optically induced decrease of positive space charge after application of the bias and infrared light. The observed energy shift of the level towards the conduction band in CZTS compared to CZT is in agreement with theoretical predictions of Varley [27]. They used first-principles calculations based on screened hybrid functionals and found that energy levels of cadmium vacancy shifted towards the conduction band when Se replaces Te in the lattice. The observed energy shift therefore also strongly indicates that the studied defect is related to Cd vacancies.

The deep level $E_1 = E_c - 0.83$ eV observed from temporal and temperature analysis is responsible for setting the electric field after the application of the bias in CZTS. Also, it is responsible for the positive space charge at steady state.

The deep level $E_3 = E_c - 0.73$ eV in CZTS could have the same origin as the deep level $E_c - 0.70$ eV in CZT material. These levels exhibit weak optically induced electron transitions from these deep levels to the conduction band.

IV. CONCLUSIONS

The deep levels in CZTS material responsible for the dynamics of the electric-field profile and electric current were analyzed by a complex approach involving the optical and temporal and temperature measurements of the electrical field using the electro-optic Pockels effect. Three electron deep levels were identified at $E_1 = E_c - 0.83$ eV, $E_3 = E_c - 0.73$ eV and $E_4 = E_c - 1.18$ eV and one hole deep level at $E_2 = E_v + 0.83$ eV. The electron deep level $E_1 = E_c - 0.83$ eV is responsible for the positive space charge in the sample. We show that the sample can be depolarized using the hole trap at $E_2 = E_v + 0.83$ eV. The electric field under the cathode starts to increase at 1050 nm (1.18 eV) due to electron transitions from the deep level at $E_4 = E_c - 1.18$ eV to the conduction band. This transfer forms the positive space charge in the sample.

The deep levels in CZTS are compared to those measured in CZT by the same methods. We observed the theoretically predicted energy shift of the second ionization level of the cadmium vacancy towards the conduction band in CZTS relative to CZT.

ACKNOWLEDGMENT

This paper was financially supported by the Grant Agency of Czech Republic (GAČR), project 102-18-06818S and student project SVV-2019-260445. This work was also supported by the U.S. Department of Energy, Office of Defense Nuclear Nonproliferation Research and Development, DNN R&D. The manuscript has been authored by Brookhaven Science Associates, LLC under Contract No. DE-SC0012704 with the U.S. Department of Energy.

REFERENCES

[1] T. Schlesinger, J. Toney, H. Yoon, E. Lee, B. Brunett, L. Franks, and R. B. James, "Cadmium zinc telluride and its use as a nuclear radiation detector material," *Materials Science and Engineering: R: Reports*, vol. 32, no. 4, pp. 103 – 189, 2001.

[2] K. Iniewski, "CZT sensors for computed tomography: from crystal growth to image quality," *Journal of Instrumentation*, vol. 11, no. 12, p. C12034, 2016.

[3] C. G. Wahl, W. R. Kaye, W. Wang, F. Zhang, J. M. Jaworski, A. King, Y. A. Boucher, and Z. He, "The polaris-h imaging spectrometer," *Nuclear Instruments and Methods in Physics Research Section A: Accelerators, Spectrometers, Detectors and Associated Equipment*, vol. 784, pp. 377 – 381, 2015, symposium on Radiation Measurements and Applications 2014 (SORMA XV).

[4] H. S. Krawczynski, D. Stern, F. A. Harrison, F. F. Kislat, A. Zajczyk, M. Beilicke, J. Hoormann, Q. Guo, R. Endsley, A. R. Ingram, H. Miyasaka, K. K. Madsen, K. M. Aaron, R. Amini, M. G. Baring, B. Beheshtipour, A. Bodaghee, J. Booth, C. Borden, M. Bttcher, F. E. Christensen, P. S. Coppi, R. Cowsik, S. Davis, J. Dexter, C. Done, L. A. Dominguez, D. Ellison, R. J. English, A. C. Fabian, A. Falcone, J. A. Favretto, R. Fernndez, P. Giommi, B. W. Grefenstette, E. Kara, C. H. Lee, M. Lyutikov, T. Maccarone, H. Matsumoto, J. McKinney, T. Mihara, J. M. Miller, R. Narayan, L. Natalucci, F. zel, M. J. Pivovaroff, S. Pravdo, D. Psaltis, T. Okajima, K. Toma, and W. W. Zhang, "X-ray polarimetry with the Polarization Spectroscopic Telescope Array (PolSTAR)," *Astroparticle Physics*, vol. 75, pp. 8–28, 2016.

[5] C. Szeles, S. E. Cameron, J. O. Ndap, and W. C. Chalmers, "Advances in the crystal growth of semi-insulating CdZnTe for radiation detector applications," *IEEE Transactions on Nuclear Science*, vol. 49, no. 5, pp. 2535–2540, Oct 2002.

[6] A. E. Bolotnikov, S. Babalola, G. S. Camarda, Y. Cui, S. U. Egarievwe, R. Hawrami, A. Hossain, G. Yang, and R. B. James, "Te inclusions in CZT detectors: New method for correcting their adverse effects," *IEEE Transactions on Nuclear Science*, vol. 57, no. 2, pp. 910–919, April 2010.

[7] J. MacKenzie, F. J. Kumar, and H. Chen, "Advancements in THM-grown CdZnTe for use as substrates for HgCdTe," *Journal of Electronic Materials*, vol. 42, no. 11, pp. 3129–3132, Nov 2013.

[8] A. Burger, K. Chattopadhyay, H. Chen, X. Ma, J.-O. Ndap, M. Schieber, T. Schlesinger, H. W. Yao, J. Erickson, and R. B. James, "Defects in CZT crystals and their relationship to gamma-ray detector performance," *Nuclear Instruments and Methods in Physics Research Section A: Accelerators, Spectrometers, Detectors and Associated Equipment*, vol. 448, no. 3, pp. 586 – 590, 2000.

[9] C. Buis, E. G. dAillon, A. Lohstroh, G. Marrakchi, C. Jeynes, and L. Verger, "Effects of dislocation walls on charge carrier transport properties in CdTe single crystal," *Nuclear Instruments and Methods in Physics Research Section A: Accelerators, Spectrometers, Detectors and Associated Equipment*, vol. 735, pp. 188 – 192, 2014.

[10] A. Bolotnikov, G. Camarda, Y. Cui, G. Yang, A. Hossain, K. Kim, and R. B. James, "Characterization and evaluation of extended defects in CZT crystals for gamma-ray detectors," *Journal of Crystal Growth*, vol. 379, pp. 46 – 56, 2013, compound Semiconductors and Scintillators for Radiation Detection Applications: A Special Tribute to the Research of Michael Schieber.

[11] G. Carini, A. Bolotnikov, G. Camarda, and R. B. James, "High-resolution X-ray mapping of CdZnTe detectors," *Nuclear Instruments and Methods in Physics Research Section A: Accelerators, Spectrometers, Detectors and Associated Equipment*, vol. 579, no. 1, pp. 120 – 124, 2007, proceedings of the 11th Symposium on Radiation Measurements and Applications.

[12] R. Gul, U. N. Roy, S. U. Egarievwe, A. E. Bolotnikov, G. S. Camarda, Y. Cui, A. Hossain, G. Yang, and R. B. James, "Point defects: Their influence on electron trapping, resistivity, and electron mobility-lifetime product in $\mathrm{CdTe}_x\mathrm{Se}_{1-x}$ detectors," *Journal of Applied Physics*, vol. 119, no. 2, p. 025702, 2016.

[13] R. Gul, U. N. Roy, G. S. Camarda, A. Hossain, G. Yang, P. Vanier, V. Lordi, J. Varley, and R. B. James, "A comparison of point defects in $\mathrm{Cd}_{1-x}\mathrm{Zn}_x\mathrm{Te}_{1-y}\mathrm{Se}_y$ crystals grown by Bridgman and traveling heater methods," *Journal of Applied Physics*, vol. 121, no. 12, p. 125705, 2017.

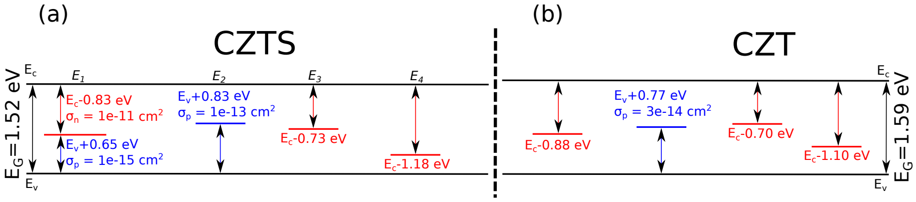

Fig. 6. Schematic of the observed energy levels with their capture cross-section determined by temperature measurements and by an infrared spectral scanning method (graph (a)). The red color represents the electron traps, and blue represents hole traps. We supplemented the scheme of the deep levels in CZT material observed in references [14], [15], [16] (graph (b)).

[14] M. Rejhon, J. Franc, V. Dědič, J. Kunc, and R. Grill, “Analysis of trapping and de-trapping in CdZnTe detectors by Pockels effect,” *Journal of Physics D: Applied Physics*, vol. 49, no. 37, p. 375101, 2016.

[15] J. Franc, V. Dědič, M. Rejhon, J. Zázvorka, P. Praus, J. Touš, and P. J. Sellin, “Control of electric field in CdZnTe radiation detectors by above-bandgap light,” *Journal of Applied Physics*, vol. 117, no. 16, p. 165702, 2015.

[16] J. Zázvorka, J. Franc, V. Dědič, and M. Hakl, “Electric field response to infrared illumination in CdTe/CdZnTe detectors,” *Journal of Instrumentation*, vol. 9, no. 04, p. C04038, 2014.

[17] V. Dědič, J. Franc, M. Rejhon, R. Grill, J. Zázvorka, and P. J. Sellin, “Depolarization of a CdZnTe radiation detector by pulsed infrared light,” *Applied Physics Letters*, vol. 107, no. 3, p. 032105, 2015.

[18] V. Dědič, J. Franc, P. J. Sellin, R. Grill, and V. Perumal, “Study on electric field in Au/CdZnTe/In detectors under high fluxes of X-ray and laser irradiation,” *Journal of Instrumentation*, vol. 7, no. issue 02, pp. P02 011–P02 011, 2012.

[19] V. Dědič, M. Rejhon, J. Franc, A. Musiienko, and R. Grill, “Space charge oscillations in semiinsulating CdZnTe,” *Applied Physics Letters*, vol. 111, no. 10, p. 102104, 2017.

[20] J. Zázvorka, J. Franc, L. Beran, P. Moravec, J. Pekárek, and M. Veis, “Dynamics of native oxide growth on CdTe and CdZnTe X-ray and gamma-ray detectors,” *Science and Technology of Advanced Materials*, vol. 17, no. 1, pp. 792–798, 2016, pMID: 27933118.

[21] M. Rejhon, J. Franc, J. Zázvorka, V. Dědič, and J. Kunc, “Influence of low-temperature annealing on schottky barrier height and surface electrical properties of semi-insulating CdTe,” *Semiconductor Science and Technology*, vol. 32, no. 8, p. 085007, 2017.

[22] K. H. Kim, J. H. Choi, A. E. Bolotnikov, G. S. Camarda, A. Hossain, G. Yang, Y. Cui, and R. B. James, “New insight into the 1.1-ev trap level in CdTe-based semiconductor,” *Journal of the Korean Physical Society*, vol. vol. 62, no. issue 4, pp. 623–627, 2013.

[23] A. Castaldini, A. Cavallini, B. Fraboni, P. Fernandez, and J. Piqueras, “Deep energy levels in CdTe and CdZnTe,” *Journal of Applied Physics*, vol. vol. 83, no. issue 4, pp. 2121–2126, 1998.

[24] M.-H. Du, H. Takenaka, and D. J. Singh, “Carrier compensation in semi-insulating Cd Te,” *Physical Review B*, vol. 77, no. 9, p. 094122, 2008.

[25] K. H. Kim, A. E. Bolotinikov, G. S. Camarda, A. Hossain, R. Gul, G. Yang, Y. Cui, J. Prochazka, J. Franc, J. Hong, and R. B. James, “Defect levels of semi-insulating Cd Mn Te,” *Journal of Applied Physics*, vol. 109, no. 11, p. 113715, 2011.

[26] J. Zázvorka, P. Hlídek, R. Grill, J. Franc, and E. Belas, “Photoluminescence of CdTe,” *Journal of Luminescence*, vol. 177, pp. 71–81, 2016.

[27] J. B. Varley, A. Samanta, and V. Lordi, “Descriptor-based approach for the prediction of cation vacancy formation energies and transition levels,” *The Journal of Physical Chemistry Letters*, vol. 8, no. 20, pp. 5059–5063, 2017, pMID: 28961000.